Cerebral Cortex, 2020;00: 1–15

doi: 10.1093/cercor/bhaa134
Original Article

ORIGINAL ARTICLE

Rapid Neuronal Ultrastructure Disruption and Recovery during Spreading Depolarization-Induced Cytotoxic Edema

Sergei A. Kirov[1,2], Ioulia V. Fomitcheva[2] and Jeremy Sword[1]

[1]Department of Neuroscience and Regenerative Medicine, Medical College of Georgia at Augusta University, Augusta, GA 30912, USA and [2]Department of Neurosurgery, Medical College of Georgia at Augusta University, Augusta, GA 30912, USA

Address correspondence to Sergei A. Kirov, Department of Neuroscience and Regenerative Medicine, Medical College of Georgia at Augusta University, 1120 15th Street, CA-3002, Augusta, GA 30912, USA. Email: skirov13@gmail.com

All authors have contributed equally to this work

Abstract

Two major pathogenic events that cause acute brain damage during neurologic emergencies of stroke, head trauma, and cardiac arrest are spreading depolarizing waves and the associated brain edema that course across the cortex injuring brain cells. Virtually nothing is known about how spreading depolarization (SD)-induced cytotoxic edema evolves at the ultrastructural level immediately after insult and during recovery. In vivo 2-photon imaging followed by quantitative serial section electron microscopy was used to assess synaptic circuit integrity in the neocortex of urethane-anesthetized male and female mice during and after SD evoked by transient bilateral common carotid artery occlusion. SD triggered a rapid fragmentation of dendritic mitochondria. A large increase in the density of synapses on swollen dendritic shafts implies that some dendritic spines were overwhelmed by swelling or merely retracted. The overall synaptic density was unchanged. The postsynaptic dendritic membranes remained attached to axonal boutons, providing a structural basis for the recovery of synaptic circuits. Upon immediate reperfusion, cytotoxic edema mainly subsides as affirmed by a recovery of dendritic ultrastructure. Dendritic recuperation from swelling and reversibility of mitochondrial fragmentation suggests that neurointensive care to improve tissue perfusion should be paralleled by treatments targeting mitochondrial recovery and minimizing the occurrence of SDs.

Key words: cytotoxic edema, dendritic spines, mitochondria, stroke, synapse, dendritic beading

Introduction

Spreading depolarizations (SDs) are waves of sustained neuronal and glial depolarization (Dreier 2011; Hartings et al. 2017) that propagate a massive disruption of ion gradients across the brain's gray matter at a velocity of 2–9 mm/min (Leão 1944; Woitzik et al. 2013). Electrophysiological data indicate that a full spectrum from short- to very long-lasting SD waves can be observed for days to weeks in patients with stroke and brain trauma (Dreier and Reiffurth 2015; Dreier et al. 2017). These real-time SD recordings, together with monitoring of cerebral blood flow (CBF) and cytotoxic edema, provided unequivocal evidence for the causal role of SDs in the development of acute human brain injury (Dreier et al. 2017; Hartings et al. 2017).

SDs arise as the pathological side effect created by a fundamental biophysical requirement to maintain a nonequilibrium steady state of the transmembrane ion distribution that is

crucial for neuronal excitability and osmotic balance (Dreier et al. 2013). SD represents the largest disturbance of the physiological ion gradients in the living brain (Dreier 2011; Hartings et al. 2017). Following their electrochemical gradients, Na^+, Ca^{2+}, and Cl^- ions influx and K^+ ions efflux the intracellular space during SD. Driven by Gibbs-Donnan forces, cells gain more Na^+ than they lose K^+ because of the high concentration of impermeant polyanions in the cytosol (Somjen 2004; Dreier et al. 2013). The accumulation of excess osmoles in the cytosol produces an osmotic gradient leading to the influx of water in the intracellular space, that is, cytotoxic edema (Van Harreveld and Khattab 1967; Van Harreveld and Malhotra 1967; Klatzo 1987; Somjen 2004; Dreier et al. 2018). Indeed, the massive ion translocations between extracellular and intracellular space during SD develop in just a few seconds with a time scale of transmembrane ion dynamics of ~0.5 s (Hubel and Dahlem 2014) and an accompanying shrinkage of the extracellular space by 50–70% (Hansen and Olsen 1980; Jing et al. 1994; Perez-Pinzon et al. 1995; Mazel et al. 2002), which reflects the onset of cytotoxic edema. Two-photon laser scanning microscopy (2PLSM) is widely used to observe cytotoxic edema as abrupt neuronal (Andrew et al. 2007; Takano et al. 2007; Murphy et al. 2008; Risher et al. 2010, 2011; Steffensen et al. 2015), and astroglial (Risher et al. 2009, 2012; Zhou et al. 2010) swellings following the fast influx of water during SD.

During ischemia, cytotoxic edema is triggered by SD (Van Harreveld 1957; Dreier et al. 2018). Previous studies of global ischemia (Murphy et al. 2008; Risher et al. 2012) have shown that ~2–4 min after ischemia onset, and before any structural changes to cellular processes, SD occurs, leading to immediate dendritic beading alongside astroglial swelling. Neuronal cytotoxic edema involves swelling of soma and dendritic beading with the distortion of dendritic spines (Murphy et al. 2008; Risher et al. 2010). This focal dendritic swelling (beading) allows a larger volume to be contained within the equivalent surface area (Budde and Frank 2010). At a given tissue spot, dendritic beading temporarily coincides with SD taking ~6 s to reach the maximum bead size (Risher et al. 2010). Cytotoxic edema is reversible at first (Fiehler et al. 2004) but is widely accepted as an important factor in acute, irreversible brain damage that occurs when cytotoxic edema persists (Kimelberg 1995; Somjen 2004; Mongin 2007). The cellular swelling coincides with SD and provides the biophysical basis for intensity changes in the magnetic resonance imaging scans in patients diagnosed with acute cerebral infarction (Dreier and Reiffurth 2015; Hartings et al. 2017). Rapid dendritic beading, which is readily detectable in real-time with 2PLSM, serves as a reliable read-out of the onset of the neuronal cytotoxic edema in preclinical animal models of neurological disorders (Risher et al. 2010; Sword et al. 2013; Steffensen et al. 2015).

SD is a mechanism leading to cytotoxic edema (Dreier et al. 2018), but very little is known about the immediate onset of SD-induced cytotoxic edema at the ultrastructural level. Likewise, virtually nothing is known about the immediate impact of SD on synaptic circuits at the ultrastructural level and their recovery when cytotoxic edema subsides. Indeed, the amplitude of dendritic structural rearrangements arising from SD-induced cytotoxic edema can only be fully appreciated after examining affected dendrites at the ultrastructural level. However, quantitative serial section electron microscopy (ssEM) studies of neurons during SD-induced cytotoxic edema and recovery were never conducted. Here, in vivo 2PLSM followed by quantitative ssEM were used to assess the integrity of dendrites in the sensorimotor cortex of urethane-anesthetized mice during SD evoked by transient bilateral common carotid artery occlusion (BCCAO) and during recovery after reperfusion and repolarization.

Materials and Methods

Animals and Surgical Procedures

All procedures followed National Institutes of Health guidelines for the humane care and use of laboratory animals and underwent yearly review by the Animal Care and Use Committee at Medical College of Georgia. The mice were bred and kept in group cages in the certified animal facilities and provided with food and water ad libitum. We used 69 mice of the *B6.Cg-Tg(Thy1-EGFP)MJrc/J* strain (JAX:007788), but only nine male and female mice of average age ~3 months passed our rigid tissue assessment criteria (stated in the "Results" section) and were analyzed with ssEM. Mice were anesthetized with an intraperitoneal injection of urethane (1.5 mg/g), the trachea was cannulated, and animals were ventilated with SAR-1000 (CWE). Body temperature was maintained at 37 °C. The depth of anesthesia, blood oxygen saturation level (>90%), and heart rate (450–650 beats/min) were monitored continuously with a MouseOx pulse oximeter (STARR Life Sciences). Implantation of the cranial window followed standard protocol (Risher et al. 2010). An optical chamber was constructed over the sensorimotor cortex by covering the intact dura with a thin layer of 1.5% agarose prepared in a cortex buffer (in mM: 135 NaCl, 5.4 KCl, 1 $MgCl_2$, 1.8 $CaCl_2$, and 10 HEPES, pH 7.3). The chamber was open for access with glass micropipettes. The Ag/AgCl pellet ground electrode (A–M Systems) was installed under the skin above the nasal bone. A 0.1 mL bolus of 5% (w/v) Texas Red Dextran (70 kDa) (Invitrogen) in 0.9% NaCl was injected into the tail vein for CBF visualization. Chemicals were from Sigma unless indicated otherwise.

Electrophysiology and BCCAO Stroke Model

The DC potential and spontaneous electrocorticographic (ECoG) activity were recorded with a glass microelectrode (1–2 MΩ) inserted next to imaged dendrites. Signals were recorded with a MultiClamp 200B amplifier, filtered at 1 kHz, digitized at 10 kHz with Digidata 1322A and analyzed with pClamp 10 (Molecular Devices).

Transient global cerebral ischemia was induced on the microscope stage by BCCAO (Murphy et al. 2008; Risher et al. 2012; Kislin et al. 2017). Briefly, an incision was made in the middle of the ventral neck, and one suture was placed around each CCA. A single SD was evoked during occlusion by applying tension to sutures, and controlled reperfusion was then achieved by releasing the tension of these sutures.

Imaging Modalities

The Zeiss LSM510NLO META multiphoton system mounted on the Axioscope 2FS microscope was used to collect images with a 40x/0.8NA water-immersion objective. The Spectra-Physics Mai-Tai laser tuned to 910 nm was used for two-photon excitation. The 3D time-lapse image stacks consisting of ~20 sections were taken at 1 µm increments across 75 × 75 µm imaging field within layer I of the sensorimotor cortex. Images were processed with Huygens deconvolution software (Scientific Volume Imaging) and analyzed with NIH ImageJ.

Laser speckle imaging was used to acquire two-dimensional maps of CBF as described elsewhere (Dunn et al. 2001; Sigler et al. 2008; Risher et al. 2010). The cortical surface was illuminated

by a 785 nm StockerYale laser, and images were collected with 4×/0.075 NA objective at 13 Hz with 20 ms exposure time using the Dalsa Pantera 1 M60 camera.

Changes in Intrinsic Optical Signal (IOS) were quantified with ImageJ plugin (Harrison et al. 2009). The cortical surface was illuminated by red light-emitting diodes (center at 635 nm). Images were collected through 4×/0.075 NA objective at 10 Hz with 100 ms exposure time using the Dalsa Pantera 1 M60 camera. Vibrotactile stimuli of 1 ms duration were delivered at 200 Hz for 1 s using a piezoelectric bending actuator. Each imaging session contained 20 trials of 4 s collected continuously for 80 s. During each trial, 15 baseline images were acquired over 1.5 s, and 15 images were acquired after hindlimb stimulation. Baseline images were integrated to create a single baseline image, and stimulation images were integrated to create a single stimulation image. Then the stimulation image was divided by the baseline image to produce a hindlimb functional map.

Electron Microscopy and Image Analysis

Mice were perfusion-fixed through the heart at 180 mmHg with mixed aldehydes (2% paraformaldehyde, 2.5% glutaraldehyde, 2 mM $CaCl_2$, 4 mM $MgSO_4$, in 0.1 M sodium cacodylate, pH 7.4). The area of intravital imaging was identified in the fixed brain with 2PLSM using the blood vasculature and the dendritic pattern as a guide and then labeled with the Statlab Klinipath Plus permanent histological marker. The region around this fiducial point was manually trimmed under a dissecting microscope, and tissue was processed with standard microwave-enhanced procedures through osmium, uranyl acetate, dehydration with a graded ethanol series, and embedding in Epon–Araldite resin (Kirov et al. 1999). Four series per each experimental condition and 12 total, containing 147–220 sections, each ~53 nm thick, were cut at a depth of intravital imaging with a diamond knife on an EM UC6 ultramicrotome (Leica), collected on pioloform-coated copper Synaptek slot grids (Electron Microscopy Sciences), and stained with uranyl acetate and lead citrate. Serial sections were photographed at 5000× with the JEOL 1230 transmission electron microscope using the UltraScan 4000 camera (Gatan). The 3D alignment, surfaced reconstructions, and analyses, blind as to condition, were completed using RECONSTRUCT software (Fiala 2005). Dendritic spines were identified and classified by standard criteria (Harris et al., 1992; Kirov et al., 1999). The density of dendritic microtubules was assessed by dividing microtubule number by area of cross-sectioned dendrite exclusive of any spines (Fiala et al. 2003). The mean number of microtubules per cross-sectional area for each dendrite was calculated from 5 equally spaced measurements along the dendrite.

Experimental Design and Statistical analyses

Statistica (StatSoft) was used for statistical analyses. A two-tailed paired *t*-test, one-way analysis of variance (ANOVA) and covariance (ANCOVA) followed by Tukey's honest significance differences (HSD) post hoc test were used to compare group means for parametric data. Mann–Whitney rank-sum test and Kruskal–Wallis ANOVA on ranks followed by Dunn's post hoc test were used to compare the differences in the median values among the groups for nonparametric data. The linear regression analysis was applied to quantify the strength of the relationship between two variables. The slopes of the regression lines were compared using the homogeneity-of-slopes model. A χ^2 test was used to analyze data arranged in contingency tables. Kolmogorov–Smirnov (K–S) test was used for statistical analysis of dendritic protrusions length. The sample size of each experimental group is given in the "Results" and "Figure legends". Data are presented as mean ± SEM, and the significance criterion was set at $P < 0.05$.

Result

A BCCAO Stroke Model Allows Examining SD-Induced Cytotoxic Edema

We utilized a BCAAO model of global ischemia to obtain samples for quantitative ssEM analyses of the impact of a single SD on dendritic ultrastructure. The procedure was performed on the microscope stage, allowing the combination of different imaging modalities with the electrophysiological recording (Figs 1 and 2). The cortical slow DC potential and spontaneous ECoG activity were recorded with a glass microelectrode (Figs 1A and 2A). Occlusion resulted in a ~90% decrease in CBF that was followed by the characteristic nonspreading depression of spontaneous ECoG activity used as a marker of ischemic onset (>80% reduction of the power spectrum amplitude (mV^2/Hz) in the 0.3–3 Hz frequency domain) (Murphy et al. 2008; Risher et al. 2010; Dreier 2011). SD followed ECoG depression after 173 ± 27 s (note that this time is given for six mice that were used for ssEM analyses). SD was detected as a large negative shift in the DC potential of 14.8 ± 3.0 mV ($n = 6$ mice). Somatosensory stimulus-evoked IOS imaging reflects hemodynamic responses that are evoked by underlying neuronal activity (Maldonado et al. 1997). A functional area responsive to the movement of the hindlimb was delineated with IOS imaging (Murphy et al. 2008) (Fig. 1B2), and the IOS response map was used to confirm loss and recovery of cortical function during occlusion and reperfusion, respectively (Fig. 1C2,D2). Two-dimensional maps of CBF were acquired by laser speckle imaging (Figs 1B3 and 2B2). This technique was used to verify the loss of CBF during occlusion (Figs 1C3 and 2C2) and return of CBF during reperfusion (Fig. 1D3).

A total of 69 mice were allocated into three experimental groups; "Sham", "SD", and "Recovery", but only nine animals passed all rigid tissue assessment standards (outlined in the next section) and were selected for quantitative ssEM analyses. The baseline imaging was conducted in all groups to confirm an unimpaired somatosensory response, intact CBF, and undamaged dendritic structure over the area of hindlimb representation, as shown in Fig. 1B2–4. Mice in the Sham group were not subjected to BCCAO, and after baseline imaging were perfusion-fixed through the heart with mixed aldehydes. Mice in the SD group were subjected to BCCAO that evoked SD (Fig. 2A). After confirmation of SD-induced dendritic beading with 3D time-lapse 2PLSM (Fig. 2C3), mice were quickly fixed by transcardiac perfusion at 4.4 ± 0.2 min of SD onset and without CBF recovery (time is given for three mice analyzed with ssEM). In the Recovery group, blood reperfusion was started at 10–15 s after the onset of BCCAO-induced SD by releasing the tension of sutures around CCAs. Dendrites were beaded by SD (Fig. 1C4). The DC potential repolarized to the baseline level after a 1.21 ± 0.4 min of sustained depolarization ($n = 3$ mice analyzed with ssEM), and these mice were perfusion-fixed at 70 ± 3.5 min of blood reperfusion. Recuperation from dendritic beading (Fig. 1D4) was accompanied by the return of IOS maps (Fig. 1D2) and by the reoccurrence of ECoG activity (Fig. 1A), suggesting recovery of synaptic circuits (Murphy et al. 2008; Xie et al. 2014). Indeed, while significant numbers of dendritic

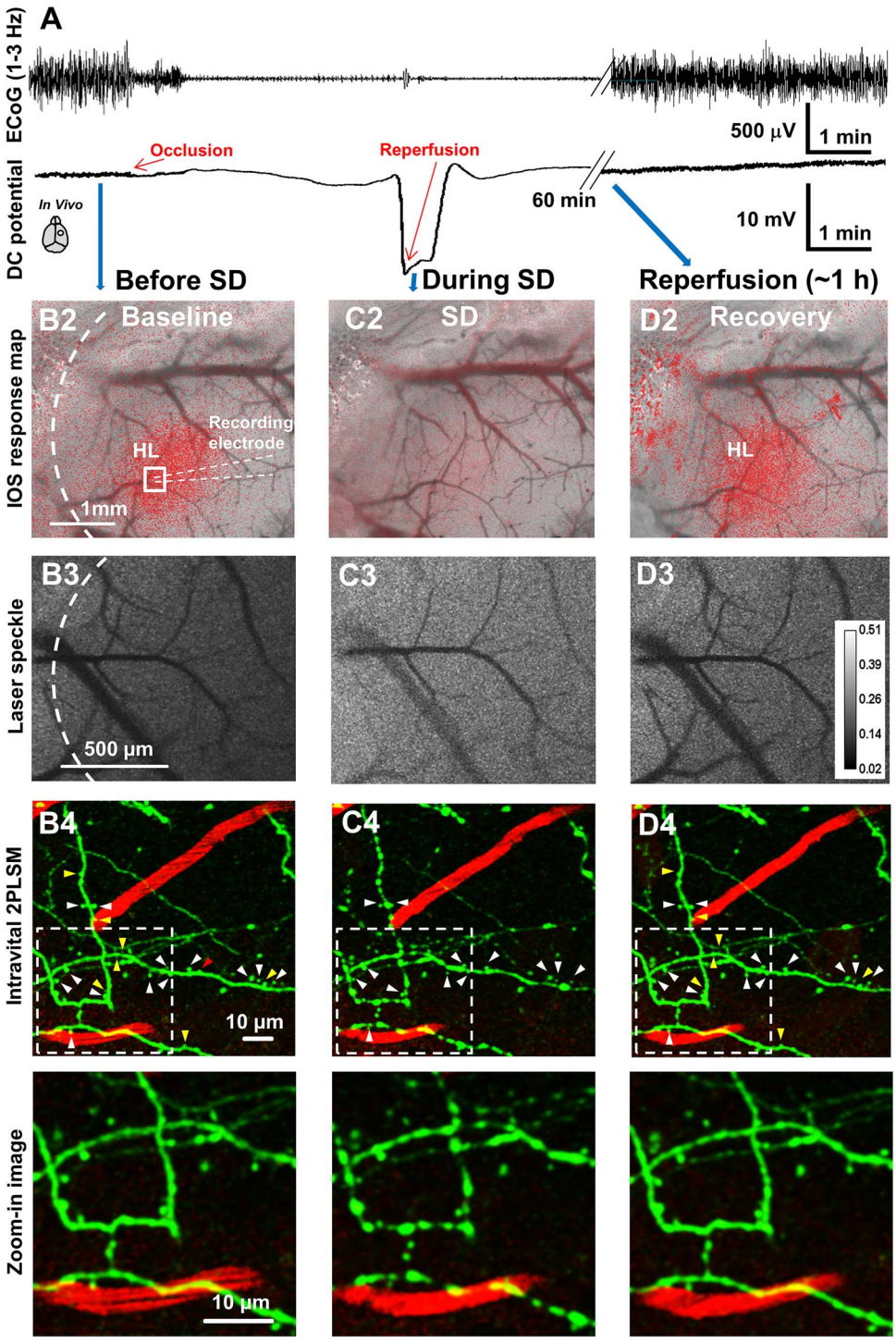

Figure 1. Experimental design to study the impact of transient BCCAO-induced SD on synaptic ultrastructure in the mouse sensorimotor cortex. (*A*) Electrocorticographic (ECoG) activity from a glass microelectrode placed next to the imaged dendrites in layer I of the sensorimotor cortex. Top, digitally filtered ECoG trace (1–3 Hz bandpass), indicating rapid suppression of spontaneous activity during BCCAO and recovery of the signal after reperfusion. Bottom, the corresponding record of the DC cortical surface potential. The large negative deflection in the DC potential indicates BCCAO-induced SD. Red arrows mark the beginning of occlusion and the start of reperfusion at 10–15 s of SD onset. Blue arrows specify approximate time points on the DC potential recording when corresponding images in columns (*B*) (Before SD/Baseline), (*C*) (During SD/SD), and (*D*) (Reperfusion/Recovery) were taken. (*B2–D2*) Composite images of the cortical surface vasculature and IOS response map. A picture of the cortical surface was taken while illuminating the cortex with a green light. Color IOS response maps are showing the sensory representation of the contralateral left hindlimb (HL) over the right sensorimotor cortex. Discrete HL territory is observed before occlusion (*B2*), IOS response maps disappeared after BCCAO (*C2*) but recovered at 1 h of reperfusion (*D2*). Edges of the craniotomy (dashed circle), placement of recording microelectrode (dotted line), and 2PLSM imaging area (square) are indicated in *B2*. (*B3–D3*) In another mouse, a representative grayscale image sequence of laser speckle contrast reveals surface CBF directly below the craniotomy, with regions of high-velocity CBF appearing dark (*B3*). Loss of CBF during occlusion (*C3*) and recovery of CBF upon reperfusion (*D3*) are seen. (*B4–D4*) In vivo 2PLSM maximum intensity projection images of dendrites (green, EGFP) along with nearby blood vessels (red, Texas Red dextran). Corresponding high-magnification zoom-in images of white boxed areas are shown at the bottom. Dendritic beading (*C4*) precisely coincided with the passage of SD recorded by a microelectrode placed next to imaged dendrites. When reperfusion was initiated within 10–15 s after the detection of SD, dendritic beading was reversible (*D4*). Arrowheads illustrate some dendritic spines that were persistent (white arrowheads), transiently lost (yellow arrowheads), or permanently lost (red arrowhead) during SD-induced dendritic beading.

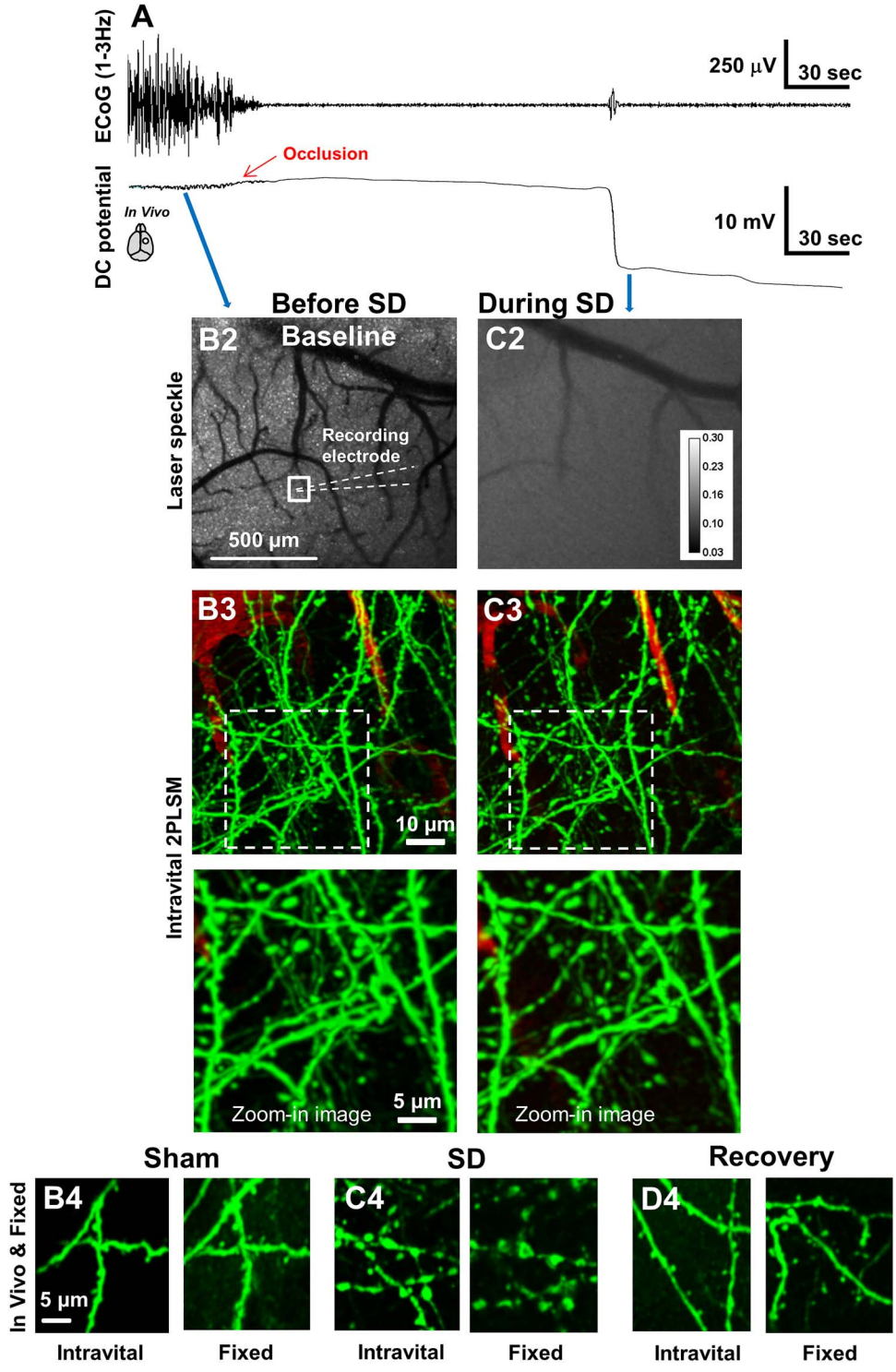

Figure 2. Experimental design to study the impact of persistent BCCAO-induced SD on synaptic ultrastructure in the mouse sensorimotor cortex. (*A*) Recordings of the ECoG activity from a glass microelectrode in the location of 2PLSM imaging in layer I of the sensorimotor cortex in the SD group of mice. Nonspreading depression of ECoG activity caused by BCCAO is shown at the top. The corresponding trace of the DC potential with persistent SD is shown at the bottom. The red arrow indicates the beginning of occlusion. Blue arrows mark approximate time points on the DC potential recording when baseline images before occlusion (column *B*) and images during persistent SD (column *C*) were acquired. (*B2*) The preocclusion baseline grayscale image of laser speckle contrast reveals flowing blood vessels that appear dark. The dotted line indicates the placement of the recording electrode, and white square marks 2PLSM imaging area. (*C2*) Corresponding laser speckle image shows the loss of CBF during occlusion. (*B3–C3*) Pairs of 2PLSM images of dendrites and blood vessels showing dendritic beading coinciding with the onset of SD. White boxes indicate the location of zoom-in images displayed at the bottom. After imaging, mice were perfusion-fixed through the heart without CBF recovery. (*B4–D4*) Pairs of 2PLSM high-magnification images of dendritic segments before and after animals were perfusion-fixed through the heart with mixed aldehydes. The same imaging fields are shown before and after fixation in sham-operated mouse (Sham group, *B4*). Nearly the corresponding imaging fields are shown before and after fixation in mouse perfusion-fixed at 4 min after SD onset (SD group, *C4*). Different imaging fields are shown after reperfusion in a mouse from the Recovery group before and after fixation (*D4*).

spines were not detectable during SD (56.4 ± 7.4% decrease in spine density, $t(19) = 5.97$, $P < 0.001$, Paired t-test, $n = 6$ mice analyzed with ssEM), spine density almost completely recovered within 97.3 ± 7.8% of the baseline values during repolarization and reperfusion ($t(7) = 2.47$, $P < 0.05$, Paired t-test, $n = 3$ mice from Recovery group that were analyzed with ssEM) (Fig. 1B4,C4,D4).

2PLSM imaging of the fixed brain revealed that fixed dendrites were morphologically intact in mice from Sham and Recovery groups (Fig. 2B4,D4) and retained beaded appearance in the SD group (Fig. 2C4). Since dendrites appeared almost identical at the end of 2PLSM imaging and after fixation (Fig. 2B4,C4,D4), suggesting that the morphology we saw was primarily due to the effect of SD and not an ischemic artifact, we concluded that the BCCAO stroke model is suitable for examining the immediate impact of single SD on synaptic circuits at the ultrastructural level. We, therefore, used this model to study onset and recovery from SD-induced neuronal cytotoxic edema at the ultrastructural level.

Selection Criteria for ssEM Analyses

Excellent tissue preservation was a prerequisite for all EM samples in three groups (Fig. 3A,B,D). Additional criteria were 1) No apparent deficit with preocclusion imaging for dendritic structure, CBF, and IOS functional response; 2) During occlusion, CBF must have dropped to ≤90% of baseline; 3) SD has occurred within 2–5 min after occlusion; 4) CBF was regained, and the IOS signal returned after reperfusion; 5) Mice in the SD group are perfusion-fixed ~4 min after SD onset; 6) Dendrites imaged in vivo and after fixation have similar morphology to rule out fixation artifact. Only 13% of mice (9 out of 69; 3 in each group) passed all these criteria and were used for quantitative ssEM analyses.

Ultrastructural Components of Dendrites Altered by SD Reveal Cytotoxic Edema

Tissue blocks from areas of 2PLSM imaging have yielded electron micrographs showing intact neuropil in Sham animals (Fig. 3A) with consistent ultrastructural changes within SD and Recovery mice (Fig. 3B,D). A representative single section electron micrograph from neuropil in the hindlimb area of Sham mice reveals healthy dendrites with well-preserved spines and synapses with compact postsynaptic densities, intact cytoplasm with uniformly spaced microtubules and structurally unimpaired mitochondria (Fig. 3A). In contrast, dendrites from the SD group have signs of neuronal cytotoxic edema with a watery cytoplasm and microtubule loss. Cross-sectioned dendritic segments contained swollen mitochondria (Fig. 3B). Likewise, longitudinally sectioned dendrites exhibited signs of focal swelling (beading) with a watery cytoplasm within beads devoid of microtubules (Fig. 3C). Electron micrographs from the Recovery group consistently show substantial recuperation of dendritic and mitochondrial structure accompanied by the repolymerization of microtubules (Fig. 3D).

Cross-sectioned dendrites were examined through serial sections to evaluate the degree of microtubule disruption. In Sham mice, in agreement with our previous findings (Fiala et al. 2003), the relationship between the cross-sectional dendrite area and microtubule number was linear. The same linear relationship relative to dendrite size remained in SD and Recovery groups (Fig. 3E). There were significantly fewer microtubules in dendrites from the SD group than in Sham mice ($P < 0.001$, Tukey's HSD), but dendritic microtubules reappear in the same number in Recovery group as in Sham ($P = 0.96$, Tukey's HSD). Indeed, average dendritic microtubule densities in the SD group decreased to 36.3 ± 4.1% ($P < 0.001$ relative to Sham, Tukey's HSD) but returned to 84.8 ± 5.0% in Recovery group ($P = 0.15$ relative to Sham, Tukey's HSD) (Fig. 3F). Thus, EM confirmed that dendritic beading and dendritic recovery, which are readily detectable in real-time with 2PLSM, are associated with substantial ultrastructural changes in dendritic cytoplasm indicative of the onset and recovery from neuronal cytotoxic edema.

Ultrastructural Changes in Spines and Synapses Alongside SD-Induced Dendritic Beading and During Recovery

Consistent with the previous report by Murphy et al. (2008), 2PLSM image analyses from the Recovery group revealed that individual spines, transiently lost during SD, reappeared in the same location, and spine density nearly entirely recovered (Fig. 1B4,C4,D4). However, some spines were lost. It is possible that these spines were not detectable with 2PLSM because they have retracted or become obscured by the dendritic shaft or by other spines. It is also feasible that SD is the mechanism implicated in the rapid spine loss, but the fate of synapses at the lost dendritic spines is unknown.

We used ssEM and unbiased volumetric analysis (Fiala and Harris 2001; Witcher et al. 2010) to quantify the fraction of synapses lost and recovered across experimental groups. At the ultrastructural level, thickened postsynaptic density (PSD) adjacent to a presynaptic axonal bouton is a characteristic of the asymmetric, presumably excitatory synapse, while uniformly thin pre- and postsynaptic densities distinguish symmetric, presumably inhibitory, or modulatory synapse. In Sham mice, asymmetric synapses were evident on dendritic spines and along some dendritic shafts. The rare symmetric synapses could also be found on some dendritic shafts. However, many synapses in the SD group had enlarged PSDs, as was previously observed after transient ischemia (Hu et al. 1998). Therefore, we did not differentiate between asymmetric and symmetric synapses because an unequivocal distinction between these classes in SD and Recovery groups was inaccurate. The unbiased 3D stereological analysis revealed that the density of synapses was not different between the groups (Fig. 4A, $P = 0.49$ one-way ANOVA). The results from the volumetric analysis were confirmed in the dendrite analyses from 3D ssEM reconstructions. The density of synapses was similar between reconstructed dendrites ($F(2,92) = 1.67$, $P = 0.19$ one-way ANOVA), demonstrating that there was no synapse loss during SD under our experimental conditions. One-way ANOVA has also revealed no differences in the density of macular ($P = 0.08$) or perforated ($P = 0.29$) synapses between groups.

Likewise, ssEM analysis revealed no changes in the density of dendritic protrusions, including shaft synapses (Fig. 4B, "All," $P = 0.46$ one-way ANOVA). However, spines and protrusions were significantly shorter in SD ($P < 0.001$, K–S test) and Recovery groups ($P < 0.001$, K–S test) than in the Sham group (Fig. 4C) indicating dendritic swelling. Next, we sorted dendritic protrusions into thin (Fig. 4D,F,H) and mushroom (Fig. 4E,G,I) spines that predominated in all conditions, or an "Other" category with stubby, branched and incomplete protrusions, filopodia, and shaft synapses. Thin and mushroom spines appeared similar in shape between groups. The density of thin spines was not

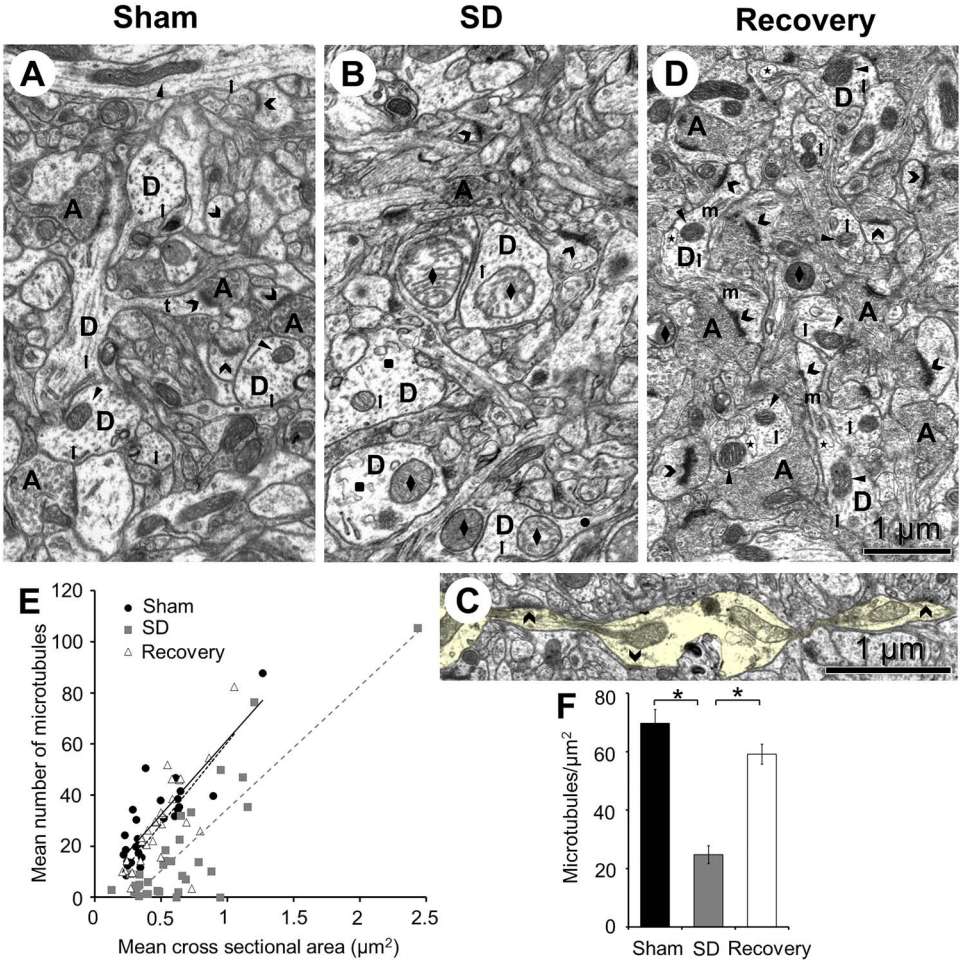

Figure 3. Representative electron micrographs from neuropil in the hindlimb territory of layer I of sensorimotor cortex at the location of intravital 2PLSM imaging. (*A*) Morphologically healthy neuropil in Sham mouse 50 µm below the pia. Dendrites [D] have intact cytoplasm with arrays of microtubules (arrows). Healthy synapses (chevrons) appose axonal boutons [A] filled with synaptic vesicles. An example of longitudinally sectioned thin (*t*) spine is also evident. Dendritic mitochondria (arrowheads) are intact. (*B*) Disrupted neuropil 40 µm below the pia at 4 min after the passage of SD (SD group). Cross-sectioned swollen dendrites [D] have watery cytoplasm (squares) and swollen mitochondria (diamonds) with some cristae damage. Fewer microtubules (arrows) occur in dendrites, and some dendritic profiles appear without microtubules. Synapses with enlarged postsynaptic densities (chevrons) appose axonal boutons partially depleted of synaptic vesicles. Narrow spine neck (circle) emanating from the main dendritic shaft [D] is visible. (*C*) Example of the longitudinally sectioned dendrite (yellow) with an undulated plasma membrane from the SD group. SD has triggered neuronal cytotoxic edema, as evidenced by dendritic beading, watery cytoplasm, and loss of microtubules. All synaptic contacts (chevrons) on this dendritic segment are located on the dendritic shaft with postsynaptic membranes still attached to the presynaptic axonal boutons. (*D*) Neuropil in Recovery group photographed 35 µm below the pia at 70 min after the onset of SD and immediate reperfusion. Cross-sectioned dendrites [D] exhibit axial arrays of microtubules (arrows) and recovered intact mitochondria (arrowheads), while few mitochondria remain swollen (diamonds). The cytoplasm of some recovered dendrites contained distended vacuoles (stars). Synapses (chevrons) with still enlarged postsynaptic densities apposed axonal boutons [A] densely packed with synaptic vesicles. Some examples of mushroom (*m*) spines are marked. (*E*) SD-induced loss and recovery of microtubule arrays in dendrites. Each point in the chart represents the mean number of microtubules and the mean cross-sectional area from five measurements along each dendritic segment reconstructed through serial sections in Sham, SD, and Recovery groups. Microtubule number was significantly reduced after SD but recovered during reperfusion ($F(2, 84) = 33.44$, $P < 0.001$, one-way ANCOVA controlling for the effect of dendritic size, Tukey's HSD post hoc test). In all groups there was a linear relationship of microtubules to the cross-sectional area of dendrites (Sham group, solid regression line, $r = 0.85$, $P < 0.001$, $n = 26$ dendrites; SD group, gray dashed regression line, $r = 0.87$, $P < 0.001$, $n = 34$ dendrites; Recovery group, dashed black line, $r = 0.74$, $P < 0.001$, $n = 28$ dendrites). The slopes of the regression lines were not different ($P = 0.3$, the homogeneity-of-slopes model for three independent samples), indicating that the loss and recovery of microtubules were similar between small and large dendrites. (*D*) Average dendritic microtubule density across experimental groups ($F(2, 84) = 42.30$, $^*P < 0.001$, one-way ANOVA with Tukey's HSD post hoc test). Data are represented as mean ± SEM.

significantly different across conditions ($P = 0.38$, Kruskal–Wallis ANOVA on Ranks) while the density of mushroom spines was 32.6 ± 9.2% less in SD than in Sham mice ($P < 0.05$, Tukey's HSD) (Fig. 4B). In contrast, the density of protrusions and synapses in the "Other" category was 112.4 ± 28.4% greater in SD than the Sham group (Fig. 4B, $P < 0.05$, Dunn's post hoc test) with no difference between other two pairs of groups.

A detailed analysis of the individual components of the "Other" category revealed a remarkable increase in the density of shaft synapses by 458.7 ± 99.0% in the SD group relative to Sham (Fig. 5A–D, $P < 0.05$, Dunn's test) suggesting that SD has induced a retraction of some spines to dendritic shafts or spines were simply overwhelmed by swelling and beading. Notably, the postsynaptic dendritic membranes remained always attached to the presynaptic axonal boutons. During Recovery, the density of shaft synapses has significantly decreased by 43.9 ± 17.9% as compared with the SD group ($P < 0.05$, Dunn's test) and, although still elevated, the density of shaft synapses was not

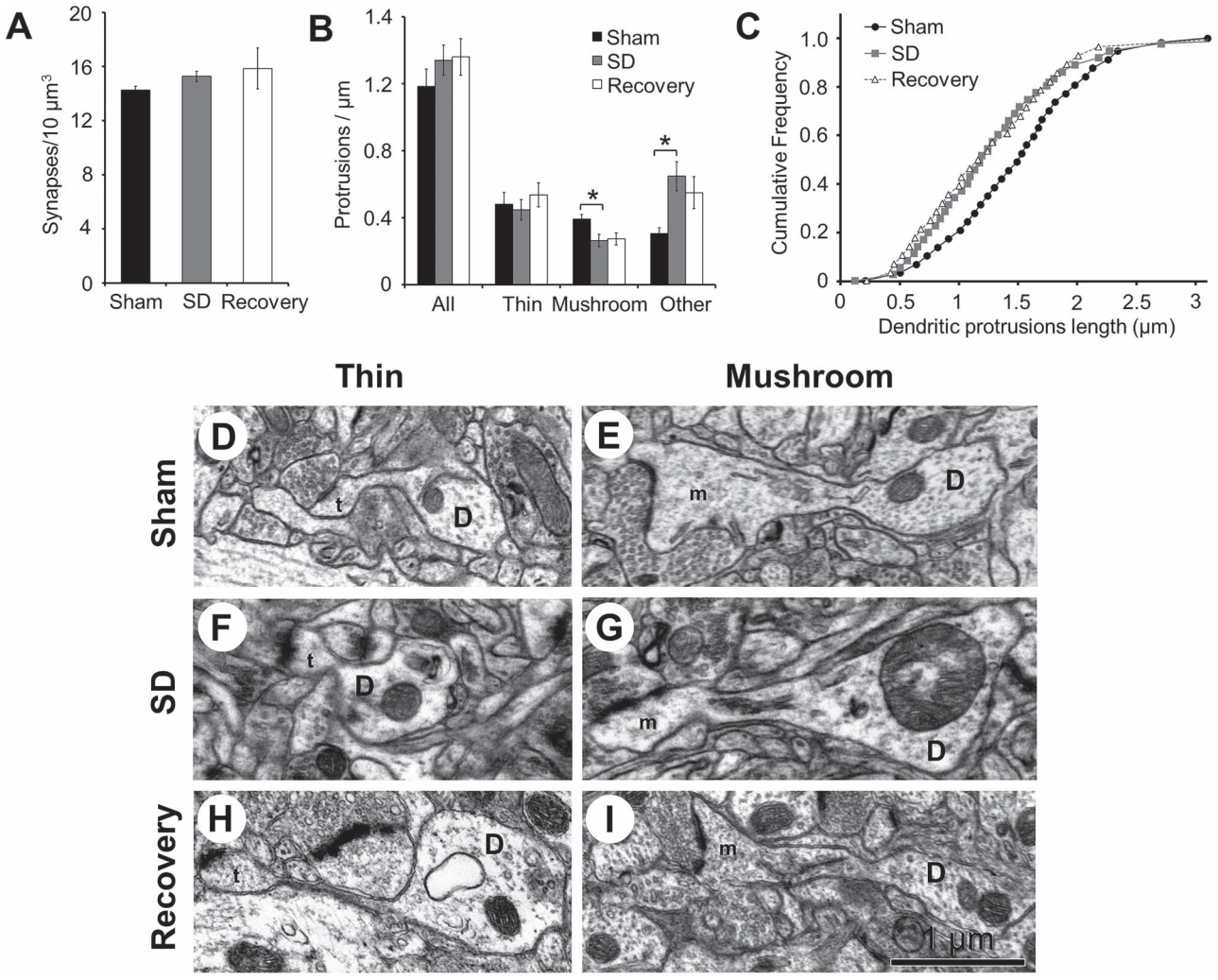

Figure 4. Synapses and dendritic protrusion number and length before, during, and after recovery from SD. (*A*) The unbiased 3D stereological analysis has shown no change in volumetric densities of synapses across groups ($F(2,9) = 0.78$, $P = 0.49$, one-way ANOVA). Overall, 1322 synapses were counted in the 3D from a total of 873 µm^3 (~293 µm^3 per group) with 433 synapses in Sham, 438 in SD, and 451 in Recovery groups. Data are represented as mean ± SEM. (*B*) The dendrite analyses from 3D ssEM reconstructions have shown no changes in the overall density of dendritic protrusions including shaft synapses ("All," $F(2,92) = 0.89$, $P = 0.46$ one-way ANOVA) and no changes in the density of thin spines ($P = 0.38$, Kruskal–Wallis ANOVA on Ranks). There was a selective decrease in the density of mushroom spines ($F(2,92) = 3.67$, $^*P < 0.05$ one-way ANOVA with Tukey's HSD post hoc test) and increase in the density of "other" protrusions in the SD group ($^*P < 0.05$, Kruskal–Wallis ANOVA with Dunn's post hoc test). Twenty-six reconstructed dendrites with 296 synapses were analyzed in Sham, 41 dendrites with 532 synapses in SD, and 28 dendrites with 327 synapses in Recovery groups. Data are represented as mean ± SEM. (*C*) Cumulative frequency plots for dendritic protrusions length in three groups. K–S test confirmed a significant difference between the curves representing data from SD and Sham or Recovery groups. (*D*, *F*, *H*) Dendrites with a thin spine in Sham (*D*), SD (*F*), and Recovery (*H*) groups. (*E*, *G*, *I*) Typical mushroom spines in Sham (*E*), SD (*G*), and Recovery (*I*) groups. (*D*, dendrite; *t*, thin spine; *m*, mushroom spine).

significantly different from Sham animals (Fig. 5D). ANOVA revealed no changes in the density of infrequent stubby ($P = 0.08$), branched spines ($P = 0.60$), filopodia ($P = 0.06$), or incomplete protrusions ($P = 0.07$), that is, protrusions that were not entirely contained within the serial sections.

Two potential caveats might affect the finding of a marked increase in shaft synapses from only 29 observations (9.8% of total) in Sham to 211 observations at 39.7% in the SD dataset ($P < 0.001$, X^2 test). First, as indicated above, we were unable to always clearly distinguish between asymmetric and symmetric shaft synapses in SD and Recovery groups due to an increase in PSD thickness. However, it is unlikely that an increase in shaft synapses in the SD group is due to a selective rise in the number of symmetric inhibitory synapses because symmetric synapses are rare and only 6 of them were observed on reconstructed dendrites from Sham dataset. The second caveat concerns nonspiny interneuron dendrites because some of them could be accidentally included in the SD dataset. Infrequent interneuron dendrites were easily identifiable in Sham mice by a prevalence of shaft synapses rather than spine synapses (Gulyas et al. 1999; Fiala et al. 2003), and, therefore, were excluded from analyses. Indeed, only 14 out of 127 dendritic segments contained within Sham series were interneuron dendrites (11% of the total, 2–5 interneuron dendritic segments per EM series). Still, nonspiny interneuron dendrites might be mistaken for dendrites of pyramidal neurons in SD mice in those cases when the majority of spines retracted to the shaft or subdued by swelling and beading. Indeed, 22% of reconstructed dendrites (9

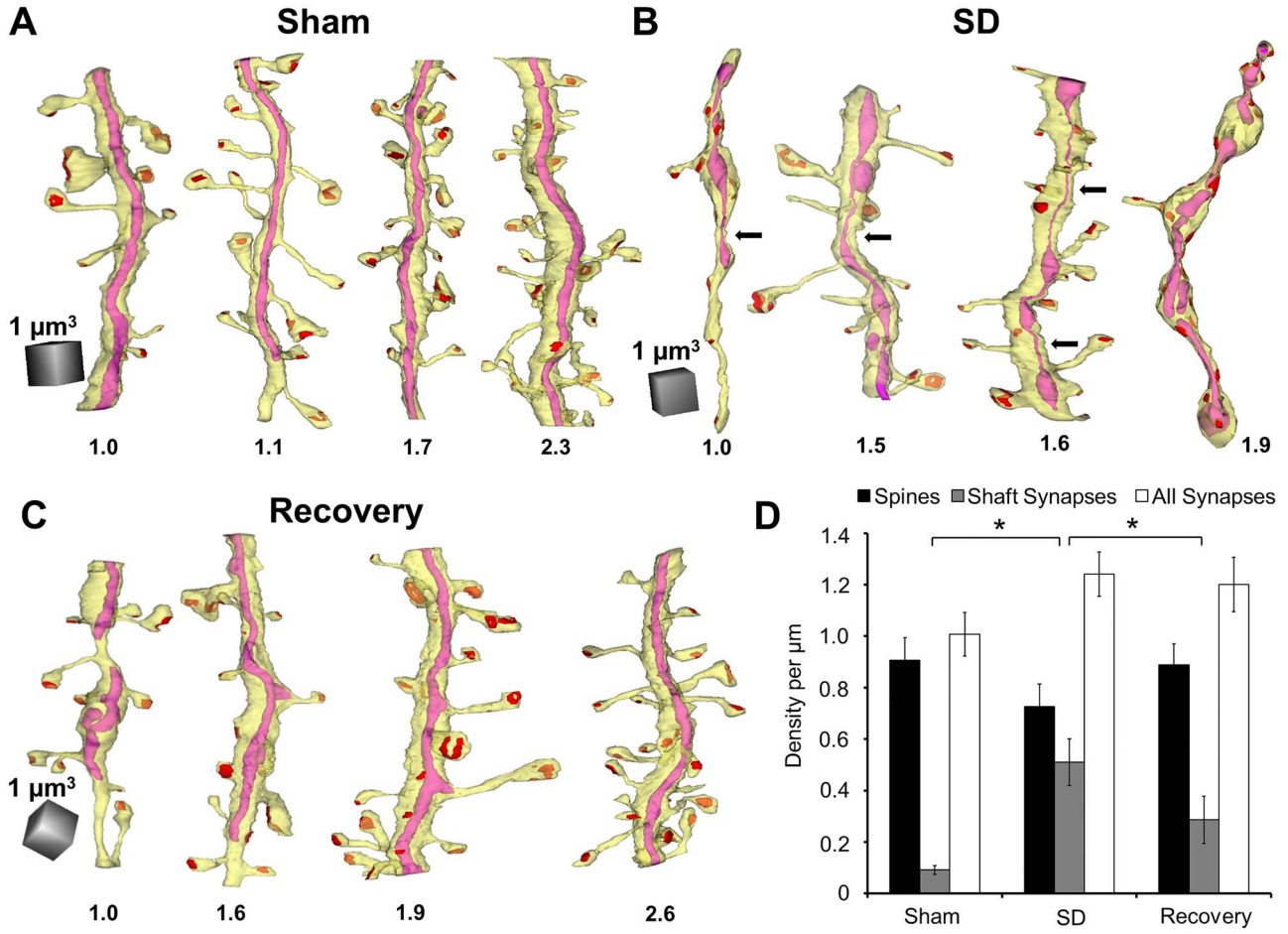

Figure 5. Transient increase in the frequency of shaft synapses during SD. (*A–C*) Examples of reconstructed dendritic segments (yellow) with excitatory synapses (red) and mitochondria (fuchsia) at the location of intravital 2PLSM imaging before (*A*), during (*B*), and after (*C*) recovery from SD. Each dendritic segment was reconstructed from 77 to 190 sections ~52 nm thick and displayed according to synapses density indicated at the bottom of each dendrite. The vast majority of synapses occurred on dendritic spines in all conditions. A fraction of shaft synapses has increased on dendrites during SD but then decreased during recovery. Dendrites from sham-operated animals contained filamentous (tubular) mitochondria, whereas mitochondria in mice fixed during SD were fragmented or contained swollen globular mitochondria interconnected by thin segments (black arrows). The majority of dendrites and mitochondria recovered at ~1 h after reperfusion. Video sequences of rotating 3D scenes containing some of these dendrites are shown in Supplementary Material. (*D*) A bar graph showing a transient increase in the density of shaft synapses during SD (*$P < 0.05$, Kruskal–Wallis ANOVA on Ranks with Dunn's post hoc test). Data are represented as mean ± SEM.

out of 41) in the SD dataset had the majority of synapses on the dendritic shaft. It is possible that some of these dendrites were nonspiny interneuron dendrites, and their intentional inclusion artificially boosted the proportion of shaft synapses in the SD dataset. To address this potential bias, we excluded all nine dendrites with predominantly shaft synapses from the SD dataset in addition to one dendrite from the Recovery dataset and repeated analyses. The density of shaft synapses was still increased in SD mice by 257.3 ± 32.7% relative to Sham (Kruskal–Wallis ANOVA on Ranks, $P < 0.05$, Dunn's test), and it was not different between Sham and Recovery groups. This additional analysis implies that SD has indeed triggered the retraction of some spines to the dendritic shaft, or these spines were overwhelmed by swelling and beading.

SD-Induced Mitochondrial Fragmentation and Recovery

As previously reported for dendrites of pyramidal neurons (Popov et al. 2005; Kislin et al. 2017), every reconstructed dendritic segment in Sham mice contained long filamentous mitochondria (Fig. 5A). Transverse serial sections of these dendritic segments allow reconstruction of 60 mitochondria with an average length of 5.79 ± 0.6 μm and a maximum width of 0.35 ± 0.01 μm (Fig. 6A). However, this average mitochondrial length is an underestimate as only 21 of reconstructed mitochondria were fully confined within series with others extending beyond one or both edges of the series. Some mitochondria were short and resembled globules in their appearance. It is well known that mitochondrial function and bioenergetics are tightly linked to their morphology and that excessive fission of normally elongated mitochondrial organelles signifies the loss of their function (Knott et al. 2008; Rugarli and Langer 2012; Picard et al. 2013; Breckwoldt et al. 2014). Therefore, we classified all reconstructed mitochondria into globules and tubules based on the ratio of the mitochondrial length to the maximum width where the ratio of 3 was arbitrarily selected as a reference threshold between these subtypes. Such analysis has shown that globular mitochondria were infrequent

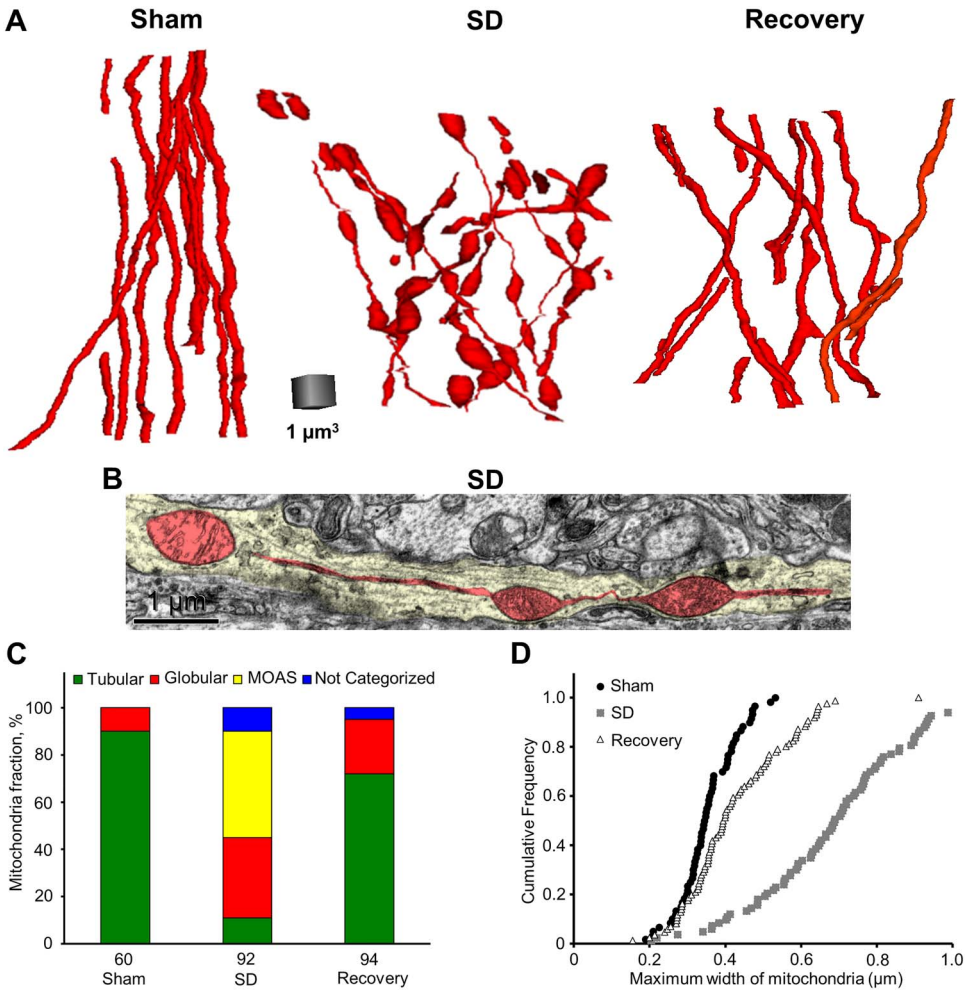

Figure 6. Mitochondria fragmentation during SD and recovery during reperfusion and repolarization. (*A*) Representative 3D mitochondrial reconstructions from ssEM reveal predominantly tubular mitochondria in Sham mice, mostly "mitochondria-on-a-string" (MOAS) and globular mitochondria during SD and again mainly tubular mitochondria in Recovery condition. Thin segments within mitochondrial organelles during SD imply ongoing fission events known to lead to the fragmentation of tubular mitochondrial network. (*B*) Representative longitudinal single EM section of a dendrite with a "mitochondria-on-a-string" in SD condition. (*C*) Percentage of mitochondrial organelles classified as tubular, globular, or MOAS in different experimental conditions. The number of mitochondria that were measured in each condition is indicated under each bar. (*D*) Cumulative frequency of maximum width of each mitochondrial organelle in Sham, SD, and Recovery datasets. The maximum width of mitochondria was significantly larger in SD than in Sham ($P < 0.0001$, K–S test) and Recovery conditions ($P < 0.0001$, K–S test) but mitochondria were still wider in the Recovery dataset than in Sham ($P < 0.005$, K–S test).

in Sham mice (10% of total) (Fig. 6C), suggesting normal fusion and fission dynamics (Westermann 2010; Chan 2012; Pernas and Scorrano 2016).

In the SD group, 92 mitochondria were reconstructed from 41 dendrites. Each dendrite contained mitochondria, but 45% of these reconstructed mitochondria appeared in the form of elongated interconnected organelles, termed "mitochondria-on-a-string" (MOAS) (Zhang et al. 2016) (Figs 5B and 6A,B). The tubular structure was retained by only 11% of mitochondria, while the frequency of globular mitochondria has increased to 34%. Remaining 10% of mitochondria were not classified because they were cut off too short at the edges of the series to categorize (Fig. 6C). MOAS were found in 71% of dendrites during SD, and the mean maximum width of enlarged MOAS segments (0.70 ± 0.02 μm, $n = 94$) was twice larger than an average maximum diameter of mitochondria in Sham animals indicating significant swelling ($P < 0.001$, Mann–Whitney rank sum test). Likewise, the maximum diameter of globular and remaining tubular mitochondria (0.60 ± 0.03 μm, $n = 45$) was significantly larger than in Sham mice ($P < 0.001$, Mann–Whitney rank sum test) (Fig. 6D). Multiple MOAS were found in 15% of dendrites, with some of them appearing to be previously interconnected segments of the same mitochondrion. This observation, together with a significantly higher proportion of globular mitochondria in SD than in Sham condition ($P < 0.001$, X^2 test), suggests ongoing fragmentation of the mitochondrial network that is considered a hallmark of mitochondrial injury (Rugarli and Langer 2012; Otera et al. 2013).

In the Recovery group, there were no MOAS found in 30 reconstructed dendritic segments (Figs 5C and 6A). Indeed, 72% of 94 reconstructed mitochondria had a tubular structure, and elongated tubular mitochondria were present in every dendrite. The fraction of globular mitochondria has decreased to 23% (Fig. 6C). However, the proportion of globular mitochondria was not significantly different from the SD group ($P = 0.07$, X^2 test) and was still significantly higher than in Sham mice

($P < 0.05$, X^2 test). The average maximum width of mitochondrial organelles in the Recovery group was 0.43 ± 0.01 µm. It was significantly less than both maximum mitochondrial and MOAS width in SD condition ($P < 0.001$, Mann–Whitney rank sum test) but still significantly larger than maximum mitochondrial width in Sham animals ($P < 0.001$, Mann–Whitney rank sum test) (Fig. 6D). Taken together, these findings indicate substantial mitochondrial recovery from SD with some residual mitochondrial swelling remaining after ~1 h of reperfusion.

Discussion

SD causes the onset of cytotoxic edema (Dreier et al. 2018). However, despite the clear clinical significance, very little information is available about the immediate development of SD-induced cytotoxic edema at the ultrastructural level. Here we presented pivotal quantitative ssEM data demonstrating the evolution of neuronal cytotoxic edema caused by SD. Quantitative ultrastructural analyses corroborated structural changes that were first observed with 2PLSM during SD. SD has triggered neuronal cytotoxic edema, as evidenced by dendritic swelling/beading with watery cytoplasm, swollen organelles, and loss of microtubules. Overall synaptic density was not affected, although the significant increase in the number of shaft synapses suggests that some spines were subdued by swelling and beading. Upon immediate reperfusion and repolarization, cytotoxic edema mainly subsides as confirmed by a nearly complete recovery of dendritic ultrastructure.

Transient global cerebral ischemia is a popular model for studying neuronal injury following short ischemic episodes. We employed a transient BCCAO model of global ischemia specifically adapted for 2PLSM imaging (Murphy et al. 2008; Kislin et al. 2017). In this model, the occurrence of a single SD coincides with dendritic beading and astroglial swelling (Risher et al. 2012), signifying a rapid onset of the cytotoxic edema (Hartings et al. 2017). Within 4 min of SD, mice were perfusion fixed through the heart, allowing a single time point snapshot of SD-induced brain edema. The unavoidable 4 min of circulatory arrest between the onset of SD and perfusion-fixation of the brain was the minimum period necessary to confirm dendritic beading with 2PLSM and perform uniform fixation procedure. While it is conceivable that ssEM analyses revealed the impact of SD-triggered edema, an additional 4 min of ischemia could further exacerbate dendritic damage. In the BCCAO model, a severe energy deficit following a sudden reduction in CBF and without prompt reperfusion results in terminal SD accompanied by permanent dendritic beading (Murphy et al. 2008). With fast reperfusion, dendritic beading subsides (Risher et al. 2012). In the Recovery group, reperfusion was started 10–15 s after SD onset, while dendritic beading and recovery were monitored with 2PLSM. Hence, ssEM analyses of the Recovery group closely reflect the recuperation of dendritic ultrastructure after the occurrence of SD-induced cytotoxic edema.

Previous single section EM analyses described neuronal ultrastructural disruptions after global ischemia and in a few hours to days after reperfusion (Pulsinelli et al. 1982; Yamamoto et al. 1990; Tomimoto and Yanagihara 1992, 1994; Zhu et al. 2017). These studies have provided only incomplete information about the degree of acute dendritic swelling and recovery, limited to a mere visual assertion of dendritic and mitochondrial swelling and disintegration of microtubules. Moreover, since electrophysiological recordings were not conducted in these studies, it is unknown if SD was triggered by ischemia and if SD invaded neuropil analyzed by EM. To our knowledge, there are only two EM studies that examined cellular swelling brought on by SD at 5–6 min after asphyxiation (Van Harreveld and Malhotra 1967) or during normoxic SD triggered by electrical stimulation or KCl application (Van Harreveld and Khattab 1967). In these studies, a murine cortical tissue was rapidly frozen and then prepared for EM with a freeze-substitution method of fixation. However, only the superficial 10–15 µm of the cortex were available for EM analyses because the fine structure of the neuropil was disrupted by ice crystals forming in a deeper tissue. While the identification of cellular elements after SD in the region of the freeze-substituted cortex was challenging, these studies revealed a profound loss of the extracellular space and the presence of swollen dendritic profiles. Some swollen dendritic structures were arising from a relatively thin fiber thus, resembling dendritic beading. It was also found that shrinkage of the extracellular space and tissue swelling was reversible after the passage of normoxic SD (Van Harreveld and Khattab 1967). Importantly, it was shown that shrinkage of the extracellular space, which reflects cytotoxic edema, did not develop with a start of ischemia, but could be detected after 5–6 min of asphyxiation, that is, about 3–4 min after SD onset (Van Harreveld and Malhotra 1967).

Our ssEM analyses revealed profound ultrastructural changes at the onset of the neuronal cytotoxic edema triggered by a global ischemia-induced SD. There is a continuous spectrum of SD waves characterized by common biophysical features ranging from the long-lasting detrimental events under severe ischemia to short-lasting harmless events in the healthy brain (Dreier 2011; Dreier and Reiffurth 2015; Hartings et al. 2017). It is conceivable that some of our ultrastructural findings such as dendritic swelling/beading are common along the entire spectrum of SD waves, including short-lasting normoxic SDs observed in intact, normally perfused brain. Indeed, dendritic beading with a transient spine loss during normoxic SD seen with in vivo 2PLSM (Takano et al. 2007; Steffensen et al. 2015; Sword et al. 2017) implies those same ultrastructural alterations as in the present study could be brought on by normoxic SD. Indeed, transient swelling of dendritic profiles during normoxic SD was observed in electron micrographs prepared by freeze-substitution (Van Harreveld and Khattab 1967). Whether normoxic SD triggers mitochondrial swelling and fragmentation deserves further study.

Our ssEM analyses revealed that all dendrites in the SD group were swollen with a different degree of beading amplitude, reflecting the differences in their initial size. Indeed, small diameter dendrites with a small surface area necessitate larger beading amplitude for a shape transformation to yield a similar increase in a volume than bigger dendrites with a larger surface area (Budde and Frank 2010). Beads often contained electron-lucent watery cytoplasm and disrupted microtubule arrays. Depolymerization of microtubules could result from a massive calcium influx during SD (Dietz et al. 2008). Still, excessive water influx might be a primary triggering mechanism of the microtubule disruption (Hoskison and Shuttleworth 2006). Uncontrolled polymerization of monomeric globular actin during energy deprivation (Atkinson et al. 2004) may lead to accumulation of filamentous actin within dendritic beads (Gisselsson et al. 2005), but we were unable to efficiently visualize the actin filament network due to the small size of microfilaments and their sensitivity to aldehydes fixation (Svitkina 2016).

Previously, we showed that SD-induced dendritic beading was not prevented with pharmacological inhibition of actin polymerization and blockade of microtubule depolymerization (Steffensen et al. 2015). These findings supported the concept that beading may result entirely from excessive water influx, but pyramidal neurons do not express functional membrane-bound aquaporins (Papadopoulos and Verkman 2013) and are largely water-impermeable under acute osmotic stress (Andrew et al. 2007). Therefore, it is unlikely that rapid dendritic beading during SD occurs as a simple osmotic event following a net gain of excess electrolytes in the neuronal cytoplasm. Quick water translocation by select neuronal chloride cotransporters as a consequence of the altered electrochemical gradients during SD emerged recently as an attractive mechanism that could explain, at least in part, rapid water influx into depolarized pyramidal neurons lacking aquaporins (Steffensen et al. 2015; Sword et al. 2017). Voltage-dependent Cl^- influx through SLC26A11 channels contributes to the onset of neuronal cytotoxic edema (Rungta et al. 2015), but the mechanism of water entry after SLC26A11 activation remains an enigma. It should be pointed out that even without SD, severely metabolically compromised neurons eventually swell due to the cation influx driven by Gibbs–Donnan forces (Somjen 2004; Dreier et al. 2013; Kirov 2014) and insufficient cation outflux caused by impaired ATP-dependent sodium and calcium pumps. However, such swelling will occur at a slower rate over minutes as compared with rapid (<6 s) SD-induced beading (Zhang et al. 2005; Risher et al. 2010; Sword et al. 2013).

The majority of dendrites recovered their shape after reperfusion and repolarization. Without a route for passive water efflux through aquaporins, the mechanism of recovery is unknown. It is conceivable that following the return of Na^+/K^+-pump function and regain of physiological ion gradients, neuronal cotransporters could contribute to recovery together with N-acetyl-L-aspartic acid molecular water pump (Baslow et al. 2007; MacAulay and Zeuthen 2010; Gagnon et al. 2013). Dendrites in the Recovery group contained uniformly spaced microtubules reassembled into normal axial arrays, and microtubule density was similar between Sham and Recovery groups. This finding is in agreement with our previous study demonstrating a remarkable ability of the dendritic microtubules to repolymerize within just a few minutes after complete disassembly (Fiala et al. 2003).

It is noteworthy that SD also generates new concentration gradients of Na^+, Cl^-, and K^+ across an intact blood–brain barrier (BBB), thus creating the driving force for extracellular ionic edema immediately following cytotoxic edema (Dreier et al. 2018). Driven by new electrochemical gradients, Na^+ and Cl^- ions enter extracellular space from the intravascular compartment creating an osmotic gradient leading to the influx of water across BBB. Furthermore, recent evidence suggests that an inverse neurovascular response to SD, that is, vasoconstriction (Dreier et al. 1998; Dreier 2011) also contributes to the ionic edema by opening the glymphatic pathway for an influx of Na^+ and water from the cerebrospinal fluid to the brain parenchyma (Mestre et al. 2020). Additionally, SD seems to contribute to the vasogenic edema that slowly develops a few hours after the ionic edema in the ischemic brain (Kang et al. 2013; Knowland et al. 2014; Sadeghian et al. 2018).

Previous in vivo 2PLSM studies revealed that SD might be a mechanism implicated in rapid distortion and loss of dendritic spines (Murphy et al. 2008; Risher et al. 2010). However, fast spine recovery (<3 min) after the passage of SD (Risher et al. 2010) suggested that some spines had merely retracted or been overwhelmed by swelling and then reappeared when beads shrank. These observations raised a key question about the fate of spine synapses when spines disappear. SsEM analyses revealed that many dendrites in the SD group were receiving synaptic contacts at swollen parts of their shafts and that the density of these shaft synapses was significantly higher than in Sham and Recovery groups. The overall density of all synapses was unchanged. Importantly, the postsynaptic dendritic membranes remained attached to the presynaptic axonal boutons explaining the ability of spines to disappear and reappear in the same locations as was observed with 2PLSM (Murphy et al. 2008; Risher et al. 2010; Zhu et al. 2017).

New spines form on mature neurons within minutes after slice preparation (Kirov et al. 1999) or during recovery from cold-induced dendritic beading (Kirov et al. 2004), after transient anoxia-hypoglycemia in vitro (Jourdain et al. 2002), or during recovery from 20 min of transient BCCAO in vivo (Zhu et al. 2017). Such synaptogenesis on mature dendrites often occurs via filopodia and immature stubby spines (Petrak et al. 2005). However, the frequency of filopodia and stubby spines was not different between Sham and Recovery groups, indicating the lack of synaptogenesis during recuperation from SD-induced cytotoxic edema under our experimental conditions.

SsEM analyses revealed profound mitochondrial swelling and fragmentation within 4 min of SD onset. It is conceivable that mitochondrial fragmentation involves rapid fission-like events. Long filamentous mitochondria detected in dendrites of Sham mice appeared in the form of MOAS in the SD group. Previously, MOAS were found in hypoxic, Alzheimer's disease, and aging brain (Zhang et al. 2016; Morozov et al. 2017) and were suggested to emerge in response to the energy depletion as a result of the fission arrest at the final steps of the fission process. In our study, the presence of MOAS and globular mitochondria that appeared previously interconnected implies ongoing fission. Excessive fission leads to mitochondrial fragmentation and release of proapoptotic factors triggering cell death (Chan 2012). It is conceivable that fragmentation was triggered and facilitated by SD either as a result of membrane permeability transition (Liu and Murphy 2009; Brenner and Moulin 2012), or disruption of mitochondria dynamics (Rugarli and Langer 2012), or both. Water accumulation during SD may also contribute to mitochondrial collapse and swelling (Greenwood et al. 2007). Future experiments are warranted to address these important questions.

The reoccurrence of tubular mitochondria in the majority of the dendrites in the Recovery group was remarkable. These findings are in agreement with intravital 2PLSM imaging, showing that fragmented mitochondria are capable of recovering after 5 min of transient BCCAO (Kislin et al. 2017). However, recovery was incomplete after more prolonged 8 min of occlusion. Full neuronal recuperation from SD is possible up to a certain point in time, termed the commitment point (Somjen 2004; Dreier 2011; Hartings et al. 2017). After the commitment point for cell death is reached, neurons will die, even if repolarization from SD is possible (Higuchi et al. 2002). Excessive mitochondrial fragmentation could be a subcellular mechanism that marks the switch between life and death during recovery from prolonged SD, and this question requires further investigation.

Conclusions and a Brief Outlook

Regarding the clinical relevance of our findings, it could be emphasized that SDs recorded in real-time over newly developing cerebral infarcts in patients (Luckl et al. 2018) share essential features with SDs recorded in the ischemic core of rodent models of focal (Oliveira-Ferreira et al. 2010; Risher et al. 2010) and global ischemia (Risher et al. 2012) such as in the present study. In particular, this includes the enormous prolongation of the negative component of the DC shift in parallel with long-lasting perfusion deficits. In this sense, our ultrastructural data provide insight into the cellular events associated with onset and recovery from SD-induced neuronal cytotoxic edema and associated destruction of synaptic circuitry. Dendritic swelling was accompanied by the enormous increase in the density of shaft synapses, indicating that some dendritic spines were overwhelmed by swelling or merely retracted. The overall density of synapses was unaffected by SD, and all synaptic connections were preserved, likely providing a substrate for recovery of somatosensory function and ECoG activity during reperfusion and repolarization when swollen dendrites shrank. Dendritic mitochondrial fragmentation develops during SD, which agrees with the previous report of mitochondrial fragmentation within minutes of injury (Kislin et al. 2017). Reperfusion was not associated with exacerbation of mitochondrial fragmentation or dendritic damage and was associated with a nearly complete recovery of dendritic ultrastructure. Dendritic recuperation from swelling and reversibility of mitochondrial fragmentation during reperfusion and repolarization suggests that future treatments to improve tissue perfusion should be combined with therapeutic interventions to minimize the probability of SDs and facilitate recovery of the mitochondrial organelle.

Supplementary Material

Supplementary material is available at *Cerebral Cortex* online.

Author Contributions

S.A.K. designed the experiments; J.S. performed the experiments and analyzed 2PLSM data; I.V.F. and S.A.K. conducted ssEM analyses; S.A.K. wrote the manuscript with input from all authors, and all authors edited and approved the manuscript before submission.

Funding

National Institutes of Health (RO1 NS083858 to S.A.K.).

Notes

The authors thank Deborah Croom for her excellent technical assistance. We thank Libby Perry and Brendan Marshall (Electron Microscopy Core at the Medical College of Georgia) for assistance with electron microscopy. *Conflict of Interest*: The authors declare no competing financial interests.

References

Andrew RD, Labron MW, Boehnke SE, Carnduff L, Kirov SA. 2007. Physiological evidence that pyramidal neurons lack functional water channels. *Cereb Cortex*. 17:787–802.

Atkinson SJ, Hosford MA, Molitoris BA. 2004. Mechanism of actin polymerization in cellular ATP depletion. *J Biol Chem*. 279:5194–5199.

Baslow MH, Hrabe J, Guilfoyle DN. 2007. Dynamic relationship between neurostimulation and N-acetylaspartate metabolism in the human visual cortex: evidence that NAA functions as a molecular water pump during visual stimulation. *J Mol Neurosci*. 32:235–245.

Breckwoldt MO, Pfister FM, Bradley PM, Marinkovic P, Williams PR, Brill MS, Plomer B, Schmalz A, St Clair DK, Naumann R *et al*. 2014. Multiparametric optical analysis of mitochondrial redox signals during neuronal physiology and pathology in vivo. *Nat Med*. 20:555–560.

Brenner C, Moulin M. 2012. Physiological roles of the permeability transition pore. *Circ Res*. 111:1237–1247.

Budde MD, Frank JA. 2010. Neurite beading is sufficient to decrease the apparent diffusion coefficient after ischemic stroke. *Proc Natl Acad Sci U S A*. 107:14472–14477.

Chan DC. 2012. Fusion and fission: interlinked processes critical for mitochondrial health. *Annu Rev Genet*. 46:265–287.

Dietz RM, Weiss JH, Shuttleworth CW. 2008. Zn2+ influx is critical for some forms of spreading depression in brain slices. *J Neurosci*. 28:8014–8024.

Dreier JP. 2011. The role of spreading depression, spreading depolarization and spreading ischemia in neurological disease. *Nat Med*. 17:439–447.

Dreier JP, Fabricius M, Ayata C, Sakowitz OW, William Shuttleworth C, Dohmen C, Graf R, Vajkoczy P, Helbok R, Suzuki M *et al*. 2017. Recording, analysis, and interpretation of spreading depolarizations in neurointensive care: review and recommendations of the COSBID research group. *J Cereb Blood Flow Metab*. 37:1595–1625.

Dreier JP, Isele T, Reiffurth C, Offenhauser N, Kirov SA, Dahlem MA, Herreras O. 2013. Is spreading depolarization characterized by an abrupt, massive release of gibbs free energy from the human brain cortex? *Neuroscientist*. 19:25–42.

Dreier JP, Korner K, Ebert N, Gorner A, Rubin I, Back T, Lindauer U, Wolf T, Villringer A, Einhaupl KM *et al*. 1998. Nitric oxide scavenging by hemoglobin or nitric oxide synthase inhibition by N-nitro-L-arginine induces cortical spreading ischemia when K+ is increased in the subarachnoid space. *J Cereb Blood Flow Metab*. 18:978–990.

Dreier JP, Lemale CL, Kola V, Friedman A, Schoknecht K. 2018. Spreading depolarization is not an epiphenomenon but the principal mechanism of the cytotoxic edema in various gray matter structures of the brain during stroke. *Neuropharmacology*. 134:189–207.

Dreier JP, Reiffurth C. 2015. The stroke-migraine depolarization continuum. *Neuron*. 86:902–922.

Dunn AK, Bolay H, Moskowitz MA, Boas DA. 2001. Dynamic imaging of cerebral blood flow using laser speckle. *J Cereb Blood Flow Metab*. 21:195–201.

Fiala JC. 2005. Reconstruct: a free editor for serial section microscopy. *J Microsc*. 218:52–61.

Fiala JC, Harris KM. 2001. Extending unbiased stereology of brain ultrastructure to three-dimensional volumes. *J Am Med Inform Assoc*. 8:1–16.

Fiala JC, Kirov SA, Feinberg MD, Petrak LJ, George P, Goddard CA, Harris KM. 2003. Timing of neuronal and glial ultrastructure disruption during brain slice preparation and recovery in vitro. *J Comp Neurol*. 465:90–103.

Fiehler J, Knudsen K, Kucinski T, Kidwell CS, Alger JR, Thomalla G, Eckert B, Wittkugel O, Weiller C, Zeumer H *et al*. 2004.

Predictors of apparent diffusion coefficient normalization in stroke patients. *Stroke*. 35:514–519.

Gagnon M, Bergeron MJ, Lavertu G, Castonguay A, Tripathy S, Bonin RP, Perez-Sanchez J, Boudreau D, Wang B, Dumas L *et al*. 2013. Chloride extrusion enhancers as novel therapeutics for neurological diseases. *Nat Med*. 19:1524–1528.

Gisselsson LL, Matus A, Wieloch T. 2005. Actin redistribution underlies the sparing effect of mild hypothermia on dendritic spine morphology after in vitro ischemia. *J Cereb Blood Flow Metab*. 25:1346–1355.

Greenwood SM, Mizielinska SM, Frenguelli BG, Harvey J, Connolly CN. 2007. Mitochondrial dysfunction and dendritic beading during neuronal toxicity. *J Biol Chem*. 282:26235–26244.

Gulyas AI, Megias M, Emri Z, Freund TF. 1999. Total number and ratio of excitatory and inhibitory synapses converging onto single interneurons of different types in the CA1 area of the rat hippocampus. *J Neurosci*. 19:10082–10097.

Hansen AJ, Olsen CE. 1980. Brain extracellular space during spreading depression and ischemia. *Acta Physiol Scand*. 108:355–365.

Harris KM, Jensen FE, Tsao B. 1992. Three-dimensional structure of dendritic spines and synapses in rat hippocampus (CA1) at postnatal day 15 and adult ages: implications for the maturation of synaptic physiology and long-term potentiation. *J Neurosci*. 12:1285–2705.

Harrison TC, Sigler A, Murphy TH. 2009. Simple and cost-effective hardware and software for functional brain mapping using intrinsic optical signal imaging. *J Neurosci Methods*. 182:211–218.

Hartings JA, Shuttleworth CW, Kirov SA, Ayata C, Hinzman JM, Foreman B, Andrew RD, Boutelle MG, Brennan KC, Carlson AP *et al*. 2017. The continuum of spreading depolarizations in acute cortical lesion development: examining Leao's legacy. *J Cereb Blood Flow Metab*. 37:1571–1594.

Higuchi T, Takeda Y, Hashimoto M, Nagano O, Hirakawa M. 2002. Dynamic changes in cortical NADH fluorescence and direct current potential in rat focal ischemia: relationship between propagation of recurrent depolarization and growth of the ischemic core. *J Cereb Blood Flow Metab*. 22:71–79.

Hoskison MM, Shuttleworth CW. 2006. Microtubule disruption, not calpain-dependent loss of MAP2, contributes to enduring NMDA-induced dendritic dysfunction in acute hippocampal slices. *Exp Neurol*. 202:302–312.

Hu BR, Park M, Martone ME, Fischer WH, Ellisman MH, Zivin JA. 1998. Assembly of proteins to postsynaptic densities after transient cerebral ischemia. *J Neurosci*. 18:625–633.

Hubel N, Dahlem MA. 2014. Dynamics from seconds to hours in Hodgkin-Huxley model with time-dependent ion concentrations and buffer reservoirs. *PLoS Comput Biol*. 10: e1003941.

Jing J, Aitken PG, Somjen GG. 1994. Interstitial volume changes during spreading depression (SD) and SD-like hypoxic depolarization in hippocampal tissue slices. *J Neurophysiol*. 71:2548–2551.

Jourdain P, Nikonenko I, Alberi S, Muller D. 2002. Remodeling of hippocampal synaptic networks by a brief anoxia-hypoglycemia. *J Neurosci*. 22:3108–3116.

Kang EJ, Major S, Jorks D, Reiffurth C, Offenhauser N, Friedman A, Dreier JP. 2013. Blood-brain barrier opening to large molecules does not imply blood-brain barrier opening to small ions. *Neurobiol Dis*. 52:204–218.

Kimelberg HK. 1995. Current concepts of brain edema. Review of laboratory investigations. *J Neurosurg*. 83:1051–1059.

Kirov SA. 2014. Astroglial and neuronal integrity during cortical spreading depolarization. In: Parpura V, Verkhratsky A, editors. *Pathological potential of neuroglia: Possible new targets for medical intervention*. Boston: Springer, p 127–153.

Kirov SA, Petrak LJ, Fiala JC, Harris KM. 2004. Dendritic spines disappear with chilling but proliferate excessively upon rewarming of mature hippocampus. *Neuroscience*. 127:69–80.

Kirov SA, Sorra KE, Harris KM. 1999. Slices have more synapses than perfusion-fixed hippocampus from both young and mature rats. *J Neurosci*. 19:2876–2886.

Kislin M, Sword J, Fomitcheva IV, Croom D, Pryazhnikov E, Lihavainen E, Toptunov D, Rauvala H, Ribeiro AS, Khiroug L *et al*. 2017. Reversible disruption of neuronal mitochondria by ischemic and traumatic injury revealed by quantitative two-photon imaging in the neocortex of anesthetized mice. *J Neurosci*. 37:333–348.

Klatzo I. 1987. Pathophysiological aspects of brain edema. *Acta Neuropathol*. 72:236–239.

Knott AB, Perkins G, Schwarzenbacher R, Bossy-Wetzel E. 2008. Mitochondrial fragmentation in neurodegeneration. *Nat Rev Neurosci*. 9:505–518.

Knowland D, Arac A, Sekiguchi KJ, Hsu M, Lutz SE, Perrino J, Steinberg GK, Barres BA, Nimmerjahn A, Agalliu D. 2014. Stepwise recruitment of transcellular and paracellular pathways underlies blood-brain barrier breakdown in stroke. *Neuron*. 82:603–617.

Leão AA. 1944. Spreading depression of activity in the cerebral cortex. *J Neurophysiol*. 7:359–390.

Liu RR, Murphy TH. 2009. Reversible cyclosporin A-sensitive mitochondrial depolarization occurs within minutes of stroke onset in mouse somatosensory cortex in vivo: a two-photon imaging study. *J Biol Chem*. 284:36109–36117.

Luckl J, Lemale CL, Kola V, Horst V, Khojasteh U, Oliveira-Ferreira AI, Major S, Winkler MKL, Kang EJ, Schoknecht K *et al*. 2018. The negative ultraslow potential, electrophysiological correlate of infarction in the human cortex. *Brain*. 141:1734–1752.

MacAulay N, Zeuthen T. 2010. Water transport between CNS compartments: contributions of aquaporins and cotransporters. *Neuroscience*. 168:941–956.

Maldonado PE, Godecke I, Gray CM, Bonhoeffer T. 1997. Orientation selectivity in pinwheel centers in cat striate cortex. *Science*. 276:1551–1555.

Mazel T, Richter F, Vargova L, Sykova E. 2002. Changes in extracellular space volume and geometry induced by cortical spreading depression in immature and adult rats. *Physiol Res*. 51(Suppl 1):S85–S93.

Mestre H, Du T, Sweeney AM, Liu G, Samson AJ, Peng W, Mortensen KN, Staeger FF, Bork PAR, Bashford L *et al*. 2020. Cerebrospinal fluid influx drives acute ischemic tissue swelling. *Science*. 367:pii: eaax7171.

Mongin AA. 2007. Disruption of ionic and cell volume homeostasis in cerebral ischemia: the perfect storm. *Pathophysiology*. 14:183–193.

Morozov YM, Datta D, Paspalas CD, Arnsten AFT. 2017. Ultrastructural evidence for impaired mitochondrial fission in the aged rhesus monkey dorsolateral prefrontal cortex. *Neurobiol Aging*. 51:9–18.

Murphy TH, Li P, Betts K, Liu R. 2008. Two-photon imaging of stroke onset in vivo reveals that NMDA-receptor independent ischemic depolarization is the major cause of rapid reversible damage to dendrites and spines. *J Neurosci*. 28:1756–1772.

Oliveira-Ferreira AI, Milakara D, Alam M, Jorks D, Major S, Hartings JA, Luckl J, Martus P, Graf R, Dohmen C *et al*. 2010.

Experimental and preliminary clinical evidence of an ischemic zone with prolonged negative DC shifts surrounded by a normally perfused tissue belt with persistent electrocorticographic depression. *J Cereb Blood Flow Metab*. 30:1504–1519.

Otera H, Ishihara N, Mihara K. 2013. New insights into the function and regulation of mitochondrial fission. *Biochim Biophys Acta*. 1833:1256–1268.

Papadopoulos MC, Verkman AS. 2013. Aquaporin water channels in the nervous system. *Nat Rev Neurosci*. 14:265–277.

Perez-Pinzon MA, Tao L, Nicholson C. 1995. Extracellular potassium, volume fraction, and tortuosity in rat hippocampal CA1, CA3, and cortical slices during ischemia. *J Neurophysiol*. 74:565–573.

Pernas L, Scorrano L. 2016. Mito-Morphosis: mitochondrial fusion, fission, and cristae remodeling as key mediators of cellular function. *Annu Rev Physiol*. 78:505–531.

Petrak LJ, Harris KM, Kirov SA. 2005. Synaptogenesis on mature hippocampal dendrites occurs via filopodia and immature spines during blocked synaptic transmission. *J Comp Neurol*. 484:183–190.

Picard M, Shirihai OS, Gentil BJ, Burelle Y. 2013. Mitochondrial morphology transitions and functions: implications for retrograde signaling? *Am J Physiol Regul Integr Comp Physiol*. 304:R393–R406.

Popov V, Medvedev NI, Davies HA, Stewart MG. 2005. Mitochondria form a filamentous reticular network in hippocampal dendrites but are present as discrete bodies in axons: a three-dimensional ultrastructural study. *J Comp Neurol*. 492:50–65.

Pulsinelli WA, Brierley JB, Plum F. 1982. Temporal profile of neuronal damage in a model of transient forebrain ischemia. *Ann Neurol*. 11:491–498.

Risher WC, Andrew RD, Kirov SA. 2009. Real-time passive volume responses of astrocytes to acute osmotic and ischemic stress in cortical slices and in vivo revealed by two-photon microscopy. *Glia*. 57:207–221.

Risher WC, Ard D, Yuan J, Kirov SA. 2010. Recurrent spontaneous spreading depolarizations facilitate acute dendritic injury in the ischemic penumbra. *J Neurosci*. 30:9859–9868.

Risher WC, Croom D, Kirov SA. 2012. Persistent astroglial swelling accompanies rapid reversible dendritic injury during stroke-induced spreading depolarizations. *Glia*. 60:1709–1720.

Risher WC, Lee MR, Fomitcheva IV, Hess DC, Kirov SA. 2011. Dibucaine mitigates spreading depolarization in human neocortical slices and prevents acute dendritic injury in the ischemic rodent neocortex. *PLoS One*. 6:e22351.

Rugarli EI, Langer T. 2012. Mitochondrial quality control: a matter of life and death for neurons. *EMBO J*. 31:1336–1349.

Rungta RL, Choi HB, Tyson JR, Malik A, Dissing-Olesen L, Lin PJC, Cain SM, Cullis PR, Snutch TP, MacVicar BA. 2015. The cellular mechanisms of neuronal swelling underlying cytotoxic edema. *Cell*. 161:610–621.

Sadeghian H, Lacoste B, Qin T, Toussay X, Rosa R, Oka F, Chung DY, Takizawa T, Gu C, Ayata C. 2018. Spreading depolarizations trigger caveolin-1-dependent endothelial transcytosis. *Ann Neurol*. 84:409–423.

Sigler A, Goroshkov A, Murphy TH. 2008. Hardware and methodology for targeting single brain arterioles for photothrombotic stroke on an upright microscope. *J Neurosci Methods*. 170:35–44.

Somjen GG. 2004. *Ions in the brain: normal function, seizures, and stroke*. New York: Oxford University Press.

Steffensen AB, Sword J, Croom D, Kirov SA, MacAulay N. 2015. Chloride cotransporters as a molecular mechanism underlying spreading depolarization-induced dendritic beading. *J Neurosci*. 35:12172–12187.

Svitkina T. 2016. Imaging cytoskeleton components by electron microscopy. *Methods Mol Biol*. 1365:99–118.

Sword J, Croom D, Wang PL, Thompson RJ, Kirov SA. 2017. Neuronal pannexin-1 channels are not molecular routes of water influx during spreading depolarization-induced dendritic beading. *J Cereb Blood Flow Metab*. 37:1626–1633.

Sword J, Masuda T, Croom D, Kirov SA. 2013. Evolution of neuronal and astroglial disruption in the peri-contusional cortex of mice revealed by in vivo two-photon imaging. *Brain*. 136:1446–1461.

Takano T, Tian GF, Peng W, Lou N, Lovatt D, Hansen AJ, Kasischke KA, Nedergaard M. 2007. Cortical spreading depression causes and coincides with tissue hypoxia. *Nat Neurosci*. 10:754–762.

Tomimoto H, Yanagihara T. 1992. Electron microscopic investigation of the cerebral cortex after cerebral ischemia and reperfusion in the gerbil. *Brain Res*. 598:87–97.

Tomimoto H, Yanagihara T. 1994. Golgi electron microscopic study of the cerebral cortex after transient cerebral ischemia and reperfusion in the gerbil. *Neuroscience*. 63:957–967.

Van Harreveld A. 1957. Changes in volume of cortical neuronal elements during asphyxiation. *Am J Phys*. 191:233–242.

Van Harreveld A, Khattab FI. 1967. Changes in cortical extracellular space during spreading depression investigated with the electron microscope. *J Neurophysiol*. 30:911–929.

Van Harreveld A, Malhotra SK. 1967. Extracellular space in the cerebral cortex of the mouse. *J Anat*. 101:197–207.

Witcher MR, Park YD, Lee MR, Sharma S, Harris KM, Kirov SA. 2010. Three-dimensional relationships between perisynaptic astroglia and human hippocampal synapses. *Glia*. 58:572–587.

Westermann B. 2010. Mitochondrial fusion and fission in cell life and death. *Nat Rev Mol Cell Biol*. 11:872–884.

Woitzik J, Hecht N, Pinczolits A, Sandow N, Major S, Winkler MK, Weber-Carstens S, Dohmen C, Graf R, Strong AJ *et al*. 2013. Propagation of cortical spreading depolarization in the human cortex after malignant stroke. *Neurology*. 80:1095–1102.

Xie Y, Chen S, Wu Y, Murphy TH. 2014. Prolonged deficits in parvalbumin neuron stimulation-evoked network activity despite recovery of dendritic structure and excitability in the somatosensory cortex following global ischemia in mice. *J Neurosci*. 34:14890–14900.

Yamamoto K, Hayakawa T, Mogami H, Akai F, Yanagihara T. 1990. Ultrastructural investigation of the CA1 region of the hippocampus after transient cerebral ischemia in gerbils. *Acta Neuropathol*. 80:487–492.

Zhang L, Trushin S, Christensen TA, Bachmeier BV, Gateno B, Schroeder A, Yao J, Itoh K, Sesaki H, Poon WW *et al*. 2016. Altered brain energetics induces mitochondrial fission arrest in Alzheimer's disease. *Sci Rep*. 6:18725.

Zhang S, Boyd J, Delaney K, Murphy TH. 2005. Rapid reversible changes in dendritic spine structure in vivo gated by the degree of ischemia. *J Neurosci*. 25:5333–5338.

Zhou N, Gordon GR, Feighan D, MacVicar BA. 2010. Transient swelling, acidification, and mitochondrial depolarization occurs in neurons but not astrocytes during spreading depression. *Cereb Cortex*. 20:2614–2624.

Zhu L, Wang L, Ju F, Ran Y, Wang C, Zhang S. 2017. Transient global cerebral ischemia induces rapid and sustained reorganization of synaptic structures. *J Cereb Blood Flow Metab*. 37:2756–2767.